S1. AERONET

AErosol RObotic NETwork – AERONET (https://aeronet.gsfc.nasa.gov/) is a network of ground-based sunphotometers that provides continuous measurement of aerosol microphysical, optical, and radiative properties (Holben et al., 1998). The key instrument, a CIMEL Electronique CE-318 sun-sky radiometer, is configured to measure direct solar irradiance at the Earth's surface at a 1.25 full field of view (FOV) every 15 minutes across eight wavelengths: 340, 380, 440, 500, 670, 870, 1020, and 1640 nm. The direct-sun measurement of AOD is combined with measurements made in hybrid and almucantar (ALM) directional scans to retrieve column-integrated aerosol microphysics and optical properties, including refractive indices, size distribution, SSA, Ångstrom exponent (AE), asymmetry parameter (g), and phase function (Sinyuk et al., 2020; Dubovik and King, 2000). The AERONET products are offered in three tiers of data processing–level 1, unscreened; level 1.5, cloud-screened and instrument-controlled; and level 2, cloud-screened, instrument-controlled, and quality-assured, and are often considered the ground truth in studies because of their high temporal resolution and low uncertainty (Xu et al., 2005; Sherman et al., 2016; Giles et al., 2019; Kumar et al., 2022). The estimated uncertainty in AERONET measured AOD, due primarily to calibration uncertainty, is ~0.01–0.02 at optical airmass of one for network field instruments, with the highest errors in the UV (Eck et al., 1999). The AERONET inversion fits the measured spectral AOD to within 0.01 consistent with the measurement accuracy of the direct sun measured AOD. A decrease in AOD will cause an increase in the uncertainty of the retrieved SSA. However, it is noted that a relaxed constraint on the spectral variation of the imaginary refractive index in future AERONET version 4 does not result in any significant change in SSA for the southern Africa BB, particular the kind documented in this study (Sinyuk et al., 2022). To minimize such uncertainties associated with the estimates of aerosol absorptivity, level 2 SSA retrievals are limited to cases where the AOD at 440 nm exceeds 0.4 (Dubovik and King, 2000; Holben et al., 2006). The uncertainty in retrieved SSA is ~0.03 at $AOD_{440} = 0.4$ and decreases at higher AOD levels (Sinyuk et al., 2020). Therefore, the number of observations differs between the direct-sun AOD products and inversion products.
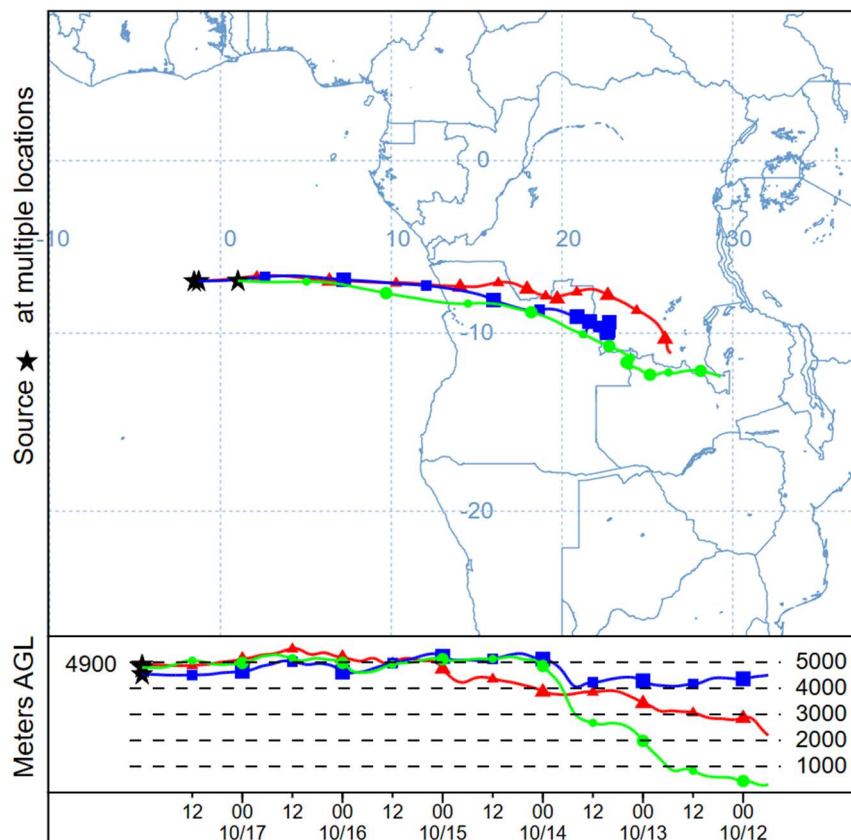
S2. HYSPLIT Trajectory

NOAA HYSPLIT MODEL
Forward trajectories starting at 0600 UTC 27 Aug 17
GDAS Meteorological Data
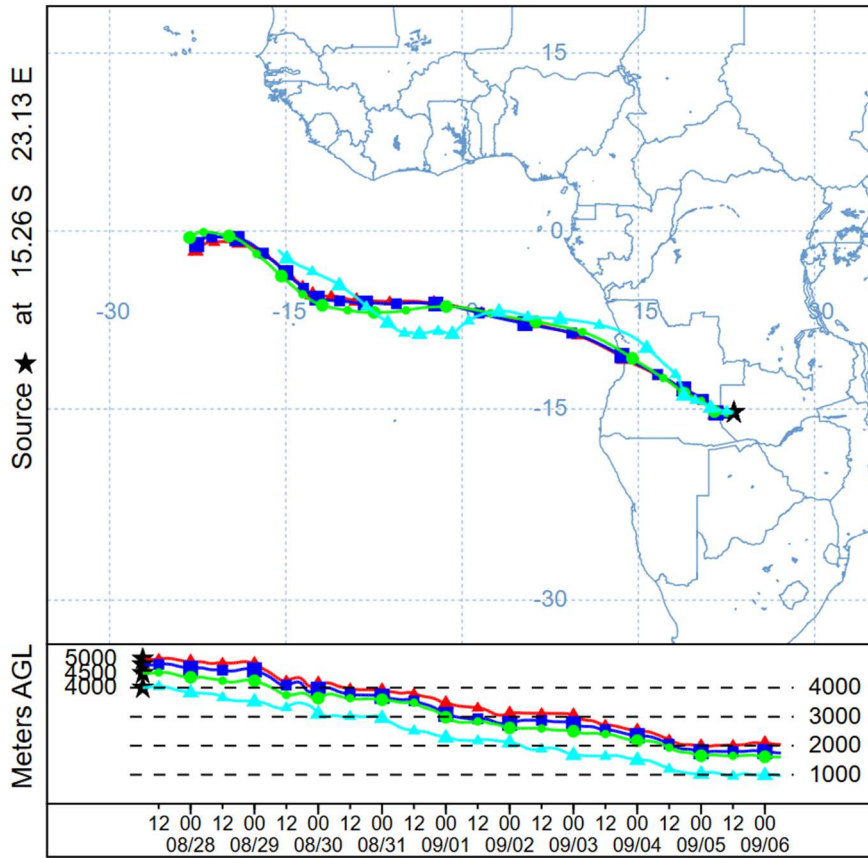
(a)

NOAA HYSPLIT MODEL
Backward trajectories ending at 0000 UTC 18 Oct 18
GDAS Meteorological Data

(b)

Figure S1: (a) Forward airmass trajectories, initiated at Mongu (-15.26, 23.13) at different altitudes on August 27, 2017. The trajectories show a consistent pathway, common among the three initiation points, converging over Ascension Island (-7.98, -14.41) after approximately 8 days. **(b)** 7-day backward trajectories ending over the SEA on October 18, 2018. The time of transport between the source region and Ascension Island in (a) is about 8-10 days, which is approximately 2 days shorter than the age estimates from the WRF-AAM model. The 2018 trajectories (b) intersect the P3 flight track on October 17, 2018, shown in Figure 1 about 12:00-13:00 UTC between 4000 – 5000m, approximately 4-6 days after departure from the source region, compared to WRF-AAM estimate of about 4-8 days (Figure 3).

3

S3. AE Thresholding

The low AE values observed in the total column over the SEA, shown in Figures 5 and 6, are likely due to the presence of BBA and coarse marine aerosols within the same column and possible mixed type of BBA and marine aerosol, as reported in (Zuidema et al., 2018; Leblanc et al., 2020; Dang et al., 2022), or the occasional intrusion of long-range transported desert dust in the FT. To address this, we implemented varying AE thresholds to systematically filter out layers with low AE values, which are indicative of the influence of coarse aerosols, thereby improving the isolation of fine-mode BBA contributions. In our analysis, we first applied the AE thresholds to the TC as shown in Fig S2, to observe how the SSA changes as different AE values are filtered. After isolating the BL using the model-derived partition ratio, we applied the AE thresholds to the FT observation.

To determine an optimal AE threshold for effectively isolating larger aerosol particles and focusing on fine particles in the SEA region, we tested four distinct AE threshold values: 0.75, 1.0, 1.2, and 1.4 and we categorized aerosol age into six bins: 0-2, 2-4, 4-6, 6-8, 8-10, and 10-12 days. The thresholding began by excluding all observations with AE values < 0.75, as shown in Fig. S2(a), and progressively increasing the threshold to eliminate observations with AE values < 1.0 (b), 1.2 (c), and 1.4 (d). As the thresholds increased, we observed a noticeable shift in the distribution of SSA across the aerosol age bins. In order to preserve a significant portion of the data from Ascension Island, where BBA likely coexist with larger particles within the MBL, we chose lower AE values for our thresholding, despite recommendations of AE ≥ 1.5 for BBA (Eck et al., 1999; 2013). Although AE values greater than 1.5 are typically expected for BBA from southern Africa (Eck et al., 2013), it is important to note that AE can decrease under certain conditions, such as fine-mode particle growth through processes like coagulation and condensation (Eck et al., 2023).

Applying various AE thresholds to the TC observations revealed a distinct change in the SSA with age. The box-whisker plot in Figure S2 displays consistent statistics across all four thresholds for the first three age bins ([0-2], [2-4], [4-6]), which correspond to samples collected near the burning sources (Mongu, Huambo). The mean SSA values for these bins are approximately 0.84, 0.86, and 0.87, respectively. The constancy in the distribution across all thresholds for these bins suggests that the AE of these samples exceeds 1.4, consistent with the characteristics of BBA in the region, as indicated by Eck et al. (2013). The application of the AE thresholds primarily impacts the distribution of older aerosols over the SEA, with each incremental increase in the threshold causing a noticeable shift in the distribution of samples in the [6-8], [8-10], and [10-12] aerosol age categories. This shift in distribution becomes particularly pronounced following the application of the fourth threshold, as seen in Figure S2 (d), where SSA peaks between 6 to 8 days of aerosol aging before declining in older age categories.
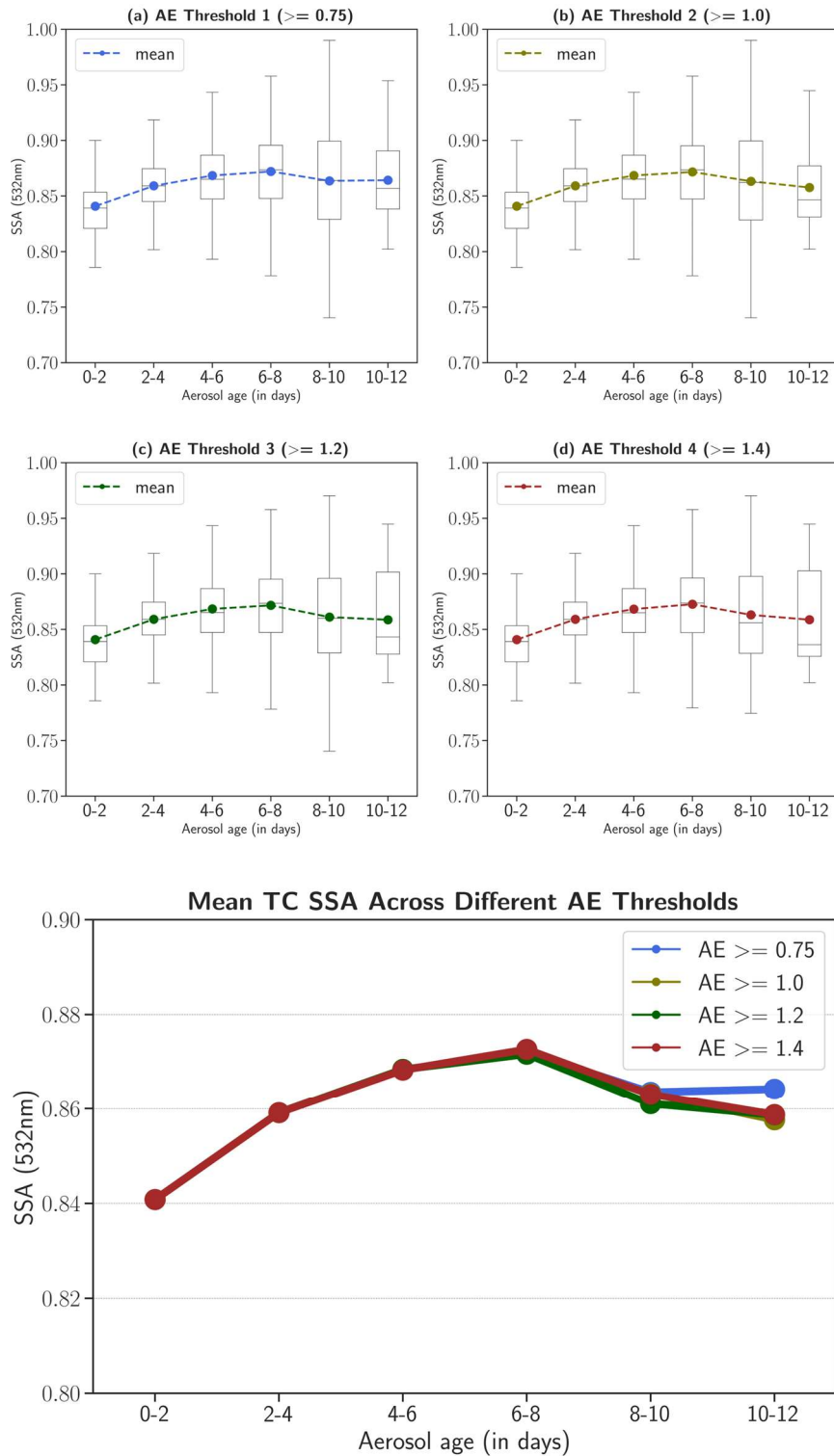
Figure S2: The evolution of SSA with aerosol age in the total column (TC), filtered with (a) AE >= 0.75, (b) AE >= 1, (c) AE >= 1.2, (d) AE >= 1.4. The box-whisker plot shows the 10th (lower whisker), 25th (lower quartile), 50th (median), 75th (upper quartile), and 90th (upper whisker) percentiles of TC SSA. The distribution of samples in age bins [0-2], [2-4],[4-6] is consistent across (a), (b), (c), and (d). The bottom panel shows the mean TC SSA for all age bins across the four thresholds.

Similar evolution patterns were observed across the different thresholds when applied to the FT. The mean FT SSA values for the first aerosol age bins remained constant at 0.84 for all four thresholds as shown in Figure S3. The [2-4], [4-6] and [6-8] age bins exhibited only minor variations for each threshold. However, a distinct temporal evolution of FT SSA for older aerosols became evident as we transitioned from the first to the final threshold. For the final threshold, the mean FT SSA for the [6-8], [8-10], and [10-12] aerosol age bins are approximately 0.87, 0.846, and 0.85 respectively. These values are marginally lower than the mean total column (TC) SSA values, indicating a higher absorption capacity of BBA within the FT over the SEA.

This result highlights two key findings: first, there is a significant contribution from coarse-mode aerosols within the atmospheric column over the SEA. Second, after excluding the cases with coarse-mode aerosols, the SSA of BBA exhibits a clear evolution as the aerosols age in the atmosphere. It is important to highlight that increasing the AE threshold from 1.2 to 1.4 led to a substantial reduction in the sample size for the [10-12] age bin, with up to 40% of observations being discarded. This suggests that the AE threshold of 1.5 or higher, recommended by Eck et al. (1999) for BBA, may primarily apply to freshly emitted particles rather than aged aerosols. To minimize data loss in the oldest age bins, we determined that an AE threshold of 1.2 serves as the optimal threshold for assessing the aging process of BBA in the SEA region.
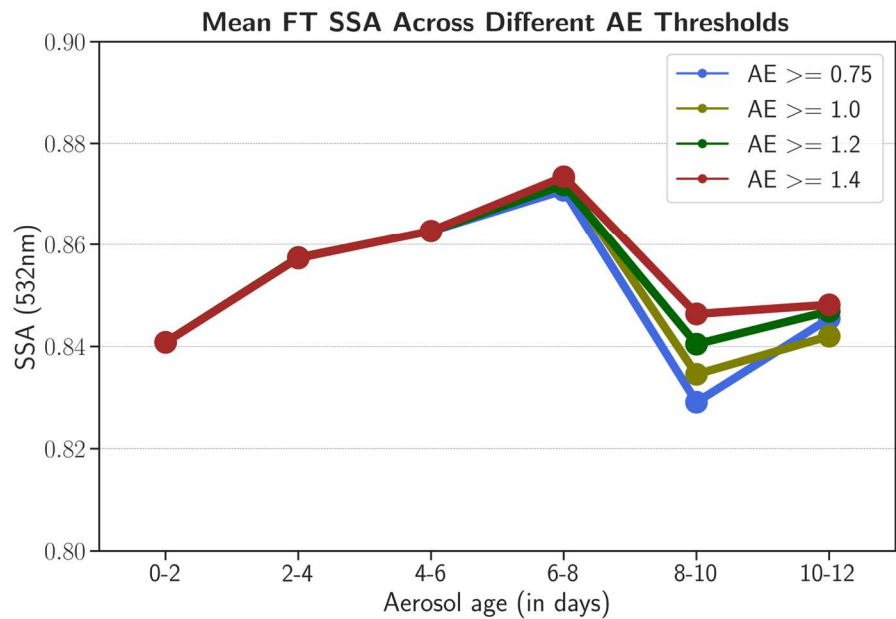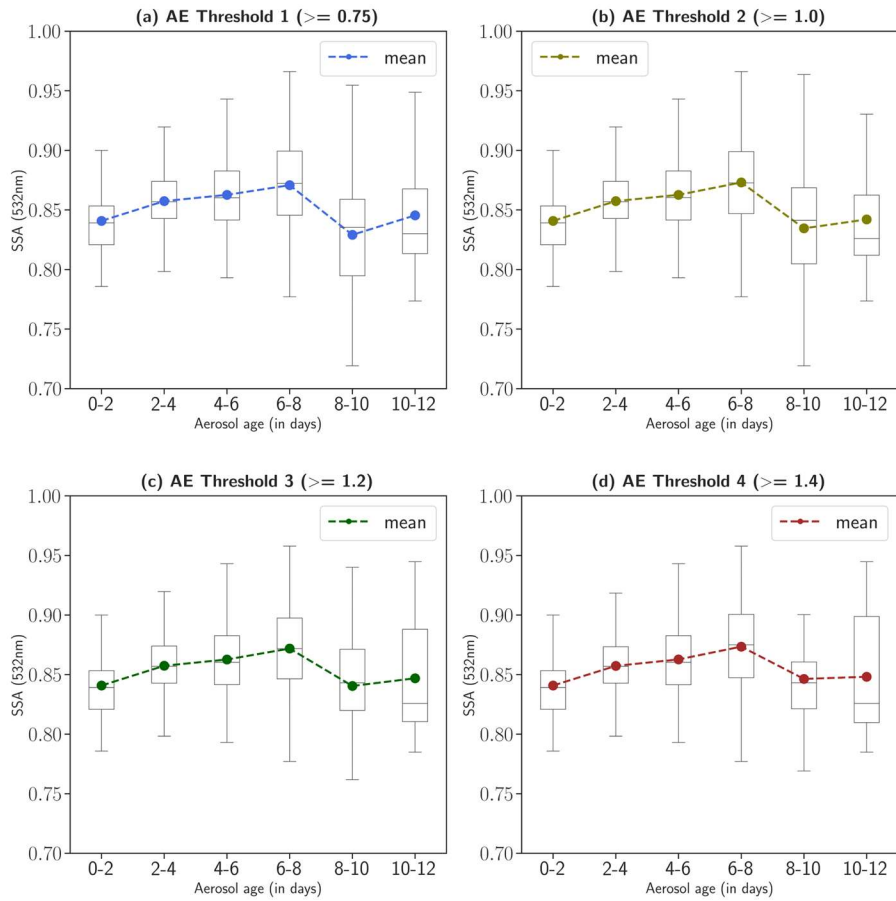
Figure S3: Same as Figure S2 but for the Free Troposphere (FT)
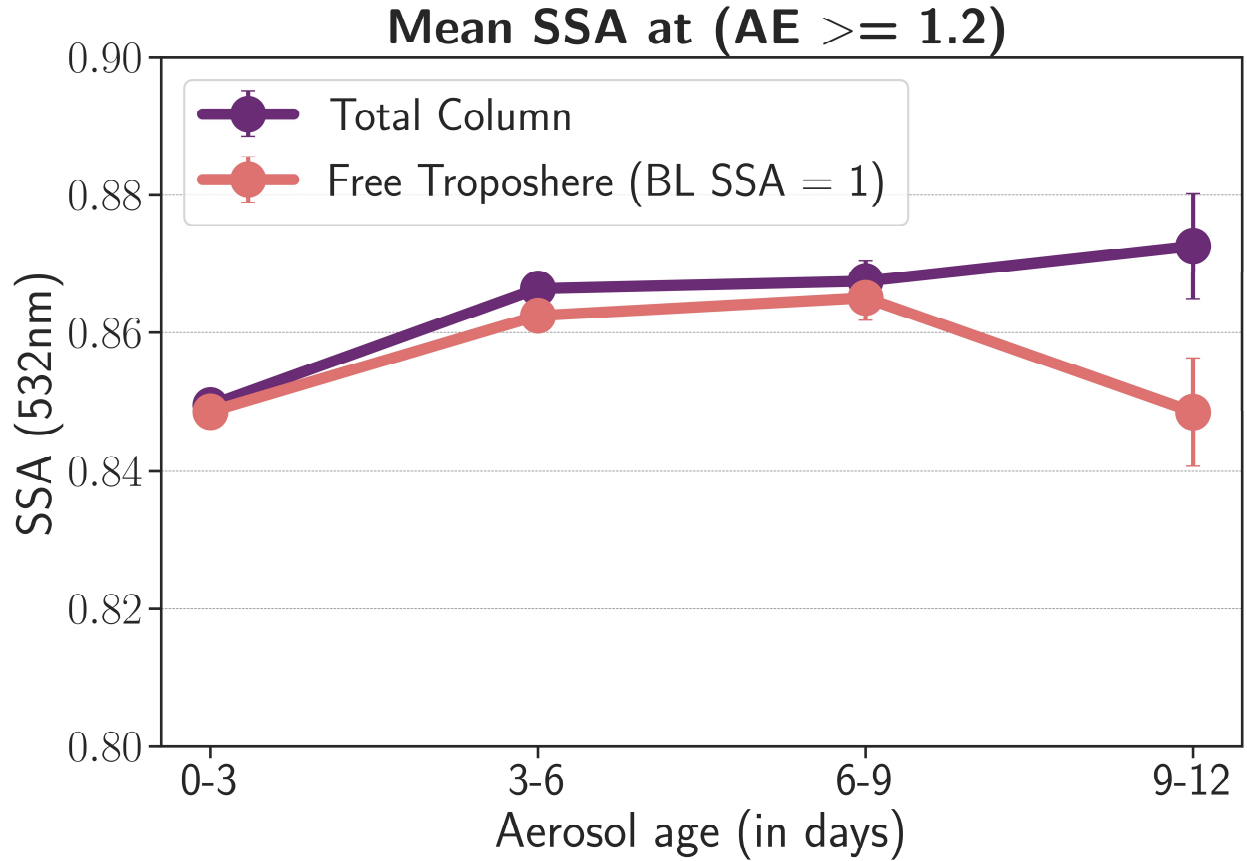
Figure S4: Comparison of the evolution of total column (TC) SSA and free tropospheric (FT) SSA across all aerosol age bins at the optimal Ångström Exponent (AE) threshold (AE ≥ 1.2), similar to Figure 13. Error bars represent the standard error of the mean. Here, we used a 3-day age bin to assess the sensitivity of FT SSA evolution to changes in the age bins.
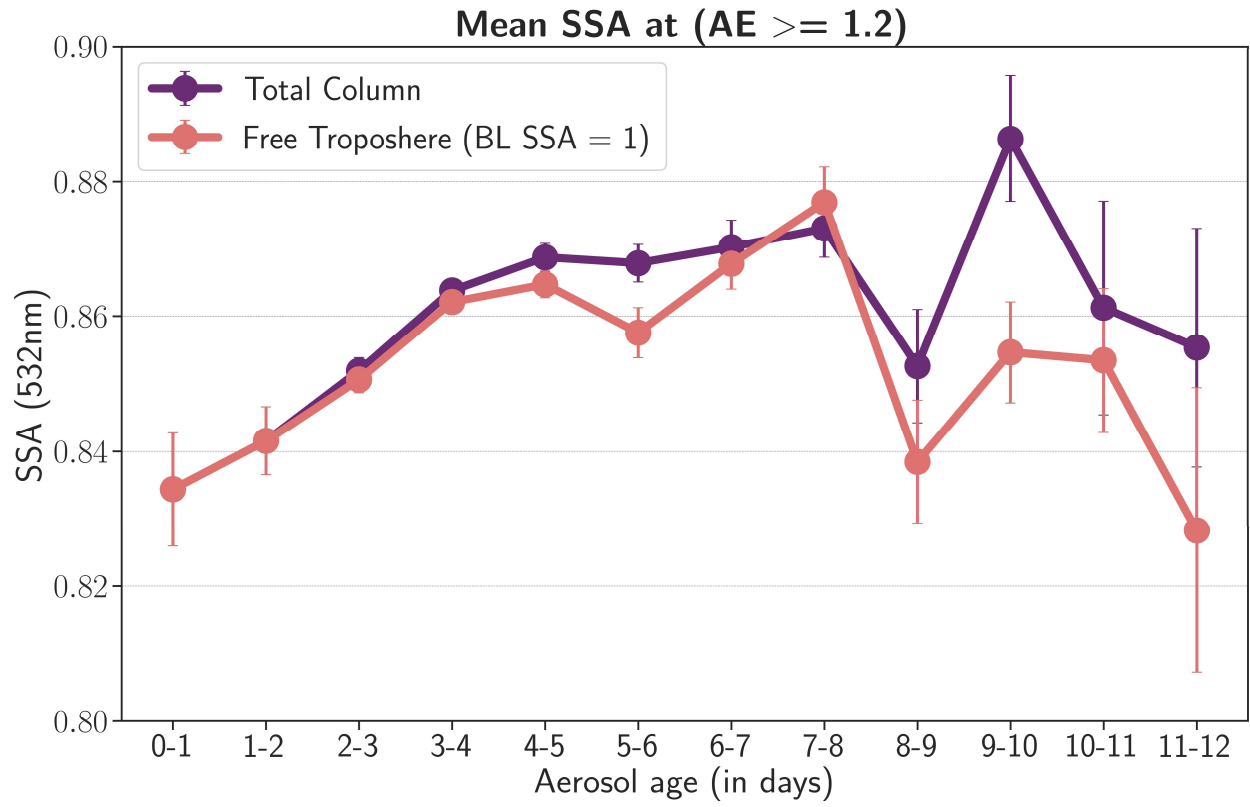
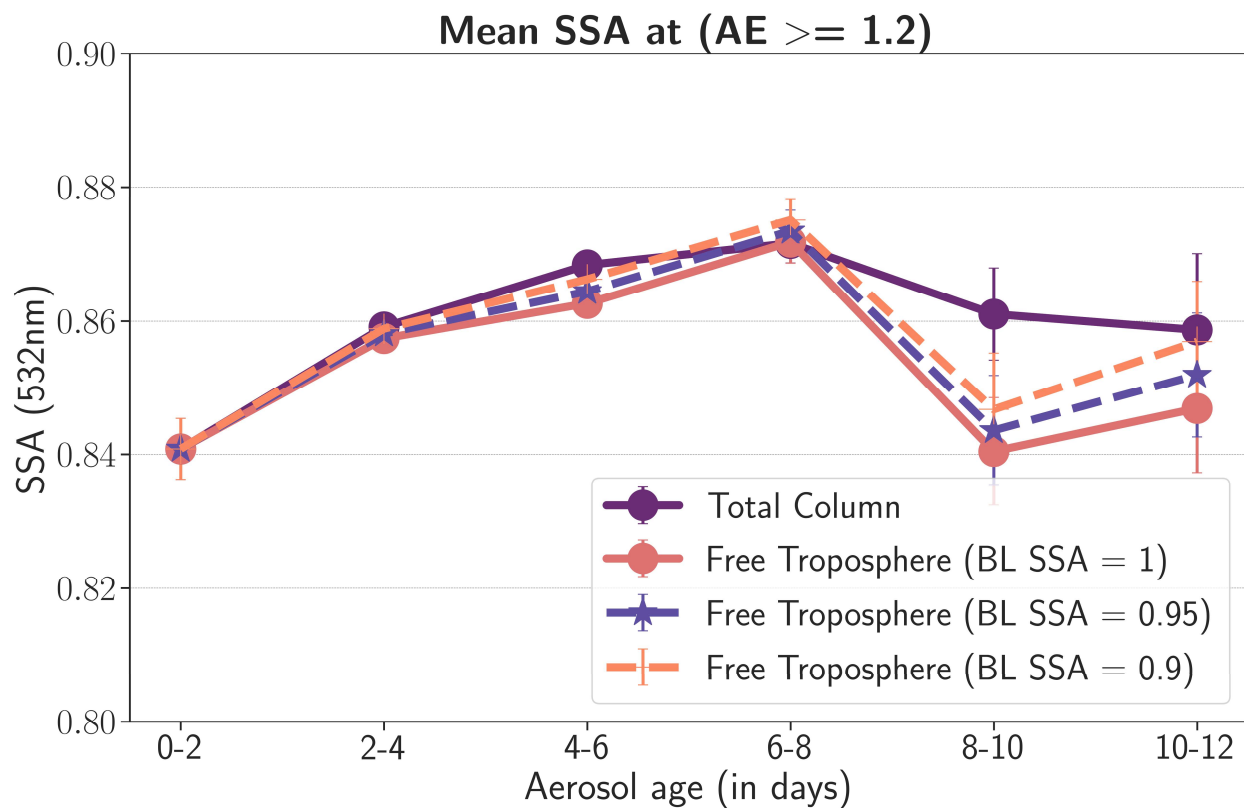**Figure S5:** Same as S4 but with 1-day age bins.

Figure S6: Comparison of the evolution of total column (TC) SSA and free tropospheric (FT) SSA across all aerosol age bins at the optimal Ångström Exponent (AE) threshold (AE ≥ 1.2), similar to Figure 13. Error bars indicate the standard error of the mean. Additionally, BL SSA values of 0.95 and 0.9 were applied to estimate FT SSA, to highlight the sensitivity of FT SSA evolution to variations in BL SSA.

Table S1: Total count of FT SSA by month for [8-10] and [10-12] day age group at (AE ≥ 1.2)

Age Group	August	September	October	Total
8-10	21	25	3	**49**
10-12	6	17	0	**23**
Total	**27**	**42**	**3**	**72**

Table S2: Total count of FT SSA by station for [8-10] and [10-12] day age group at (AE ≥ 1.2)

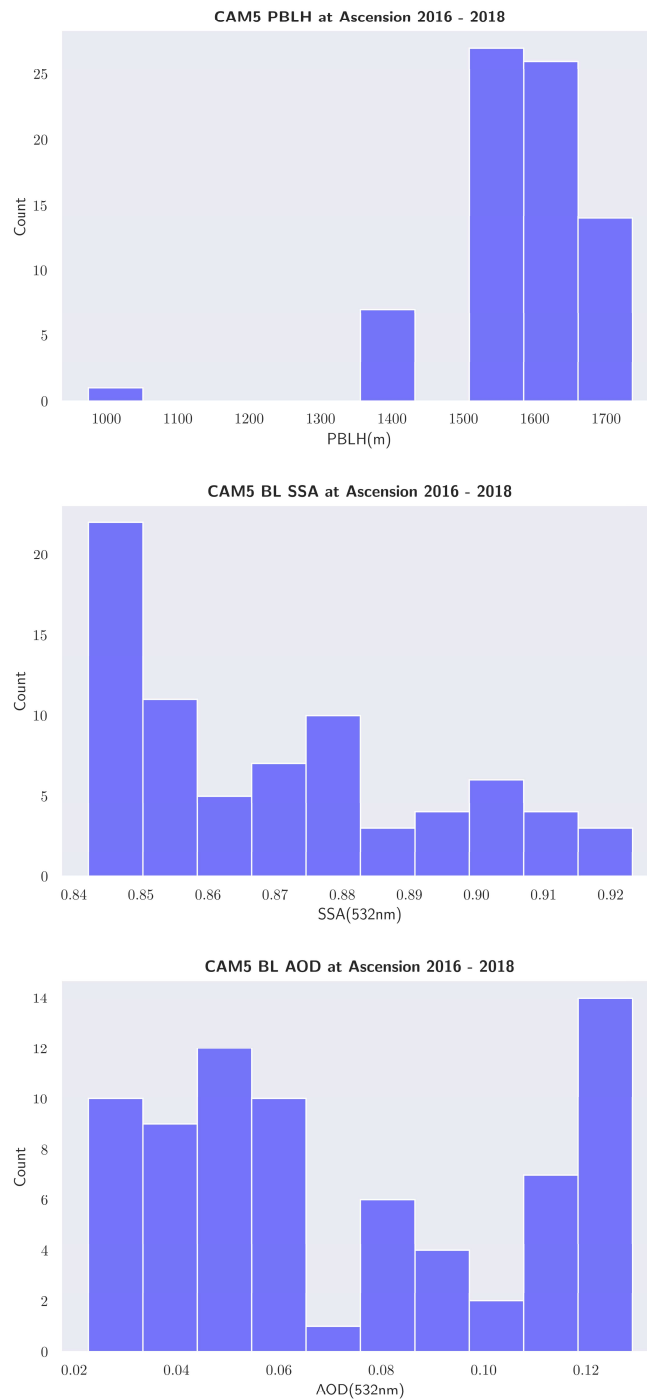| Age Group	Ascension	Namibe	Huambo	Mongu	4STAR	Total
8-10	6	6	0	0	37	**49**
10-12	11	0	0	0	12	**23**
Total	**17**	**6**	**0**	**0**	**49**	**72**

S5. Collocated WRF-CAM5 Output

Figure S7: Histograms showing the distribution of WRF-CAM5 PBLH values (top panel), WRF-CAM5 BL SSA (middle panel), and WRF-CAM5 BL AOD (bottom panel) for Ascension Island. BL SSA and BL AOD are underestimated by WRF-CAM5.
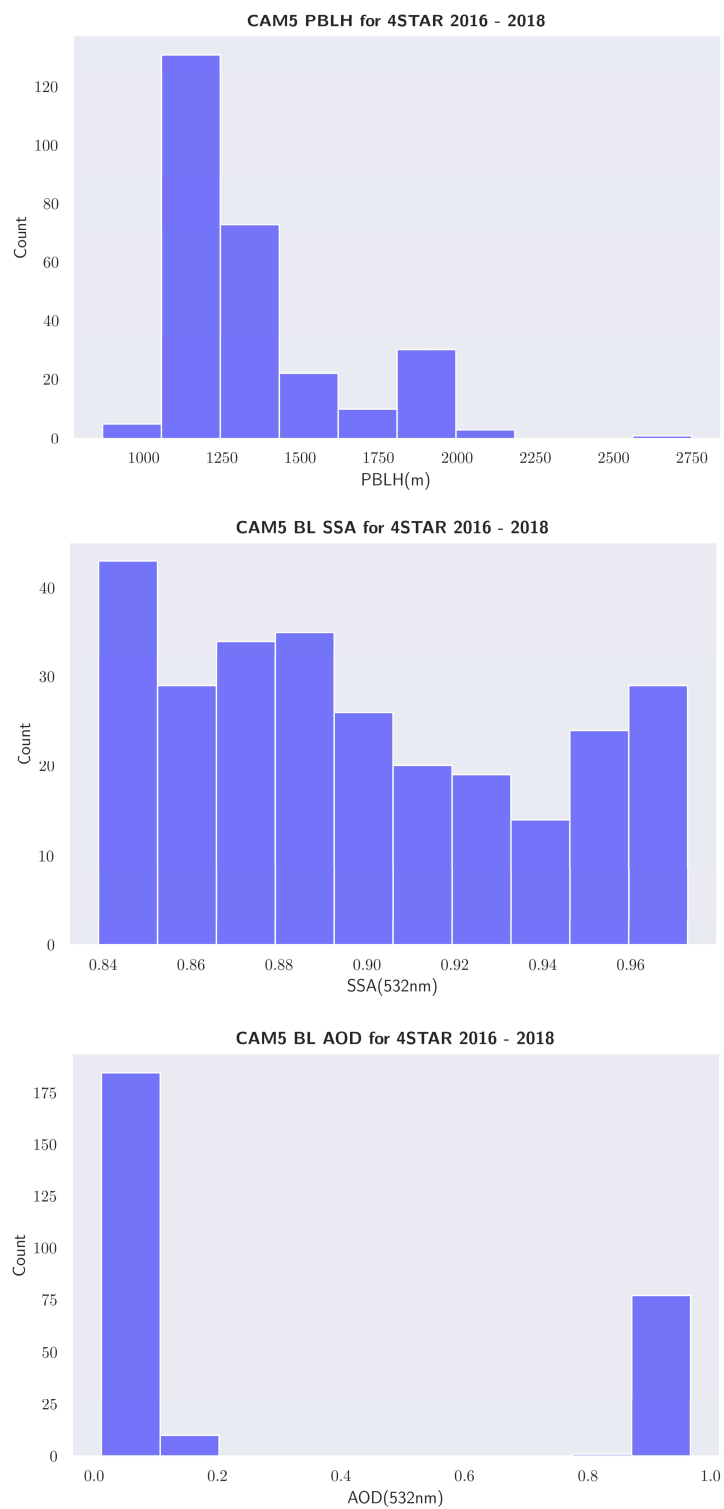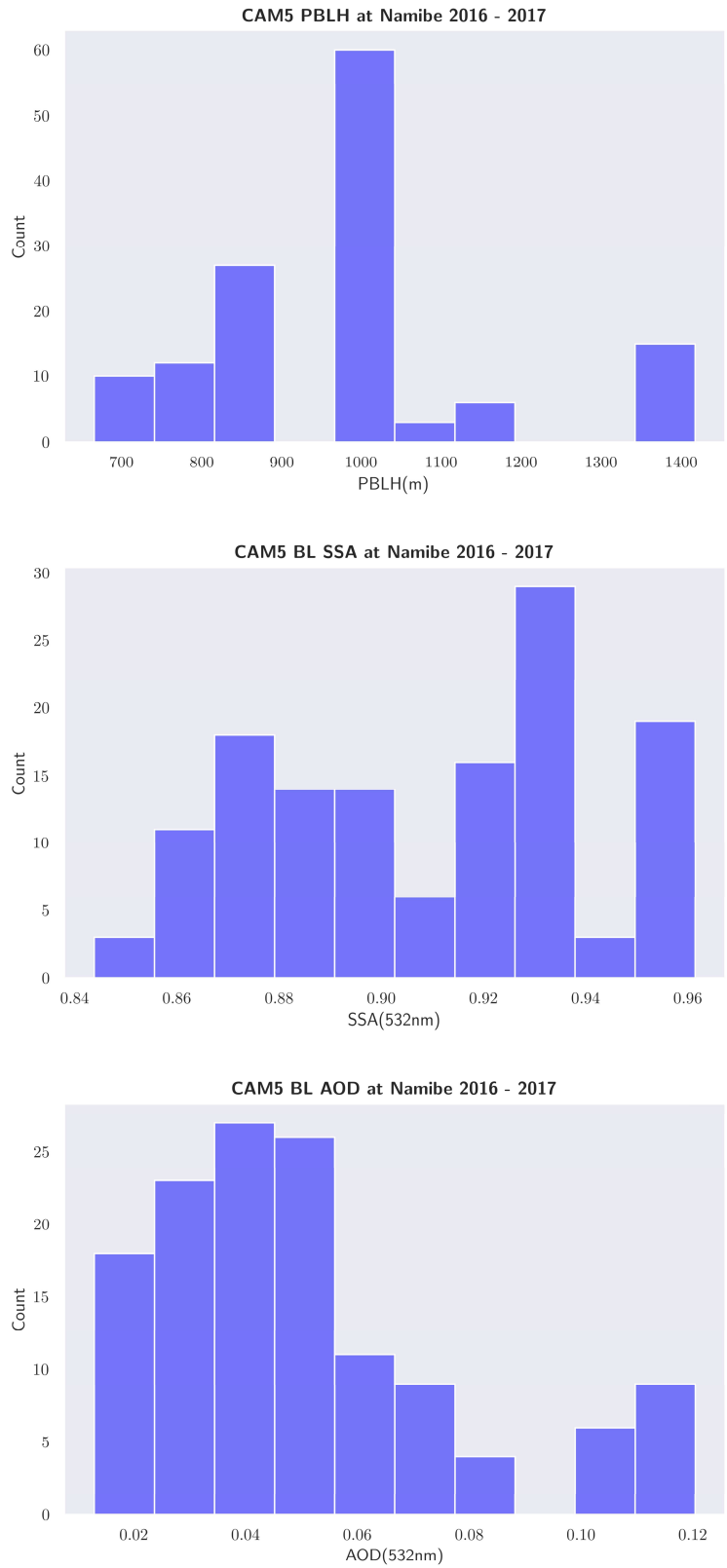
Figure S8: Same as Figure S7, but for 4STAR observations.

Figure S9: Same as Figure S7, but for Namibe observations.

14

Figure S10: NASA P3-B aircraft flight track over the SEA on October 17, 2018
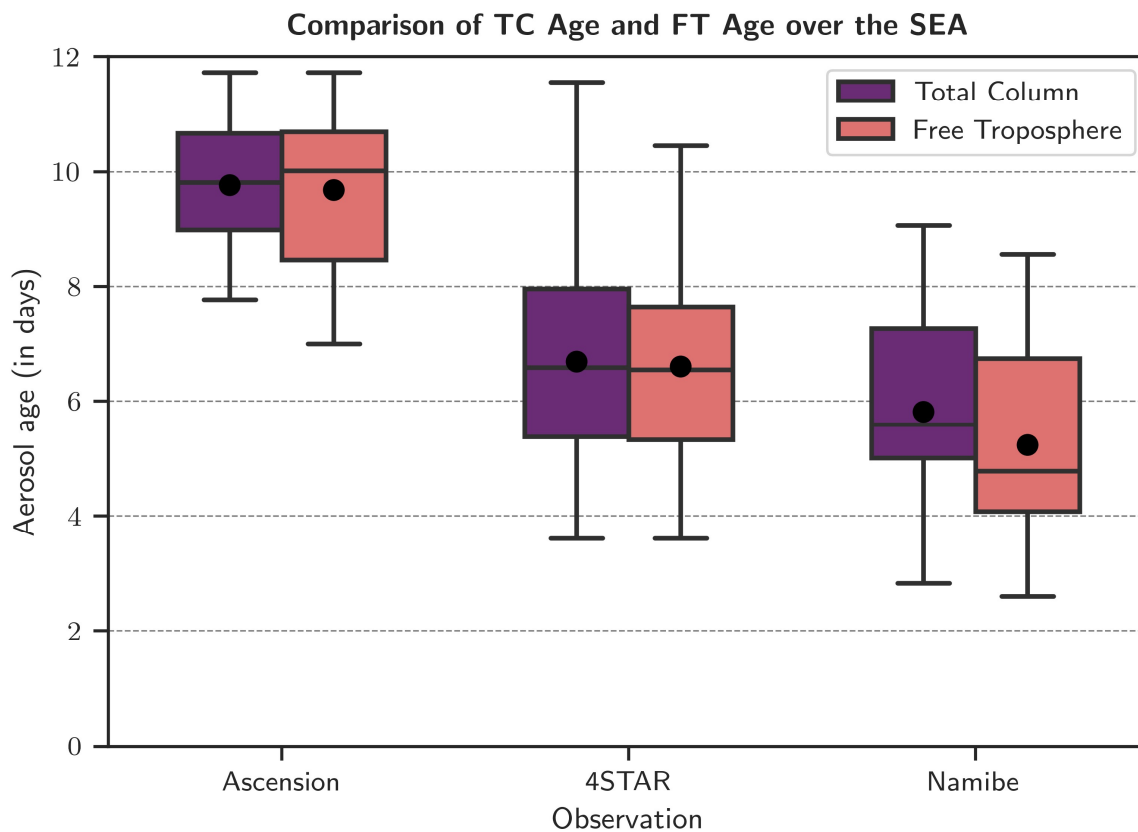
Figure S11: Comparison of aerosol age in the total column (TC) and free troposphere (FT) over the southeast Atlantic (SEA) ocean. The box-whisker plot shows the 10th (lower whisker), 25th (lower box), 50th (median), 75th (upper box), and 90th (upper whisker) percentiles. Solid black circles represent mean age values.

S6. Plume Age Variability

The assigned plume age (mean of the tracer concentration in WRF-AAM) within the column is not excessively variable. As examples for Ascension Island below. The distribution of plume age on September 02, 2016, at 15:59:52 UTC is shown in Figure S12a, and the vertical profile of plume age is shown in Figure S12(b). The PBLH value (from WRF-CAM5) at the time is 1540m. The extinction-weighted aerosol age, based on equation (1), for the AERONET measurement at the time is approximately 10 days in the TC and 10.7 days (approx. 11 days) in the FT.
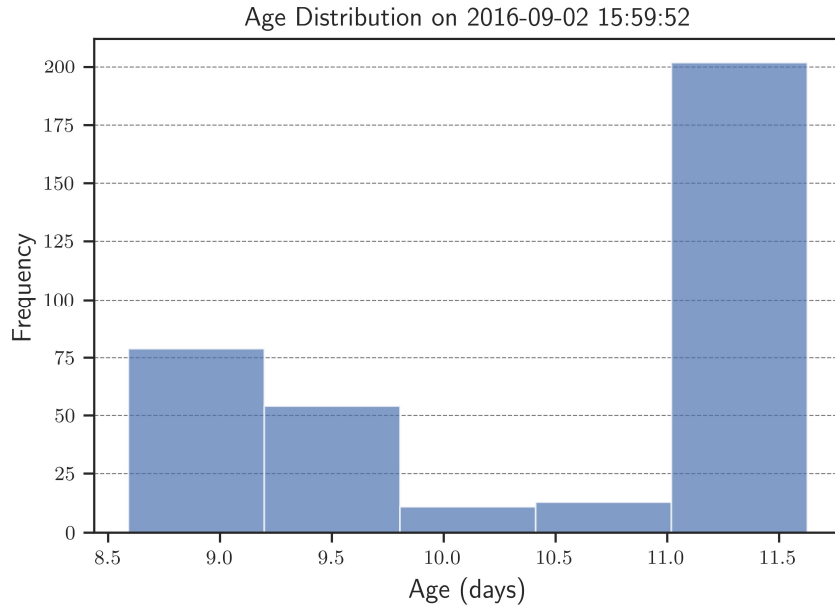

Figure S12(a): Distribution of plume age (mean of CO tracer concentrations) in the vertical at Ascension on September 02, 2016, at 15:59 UTC.
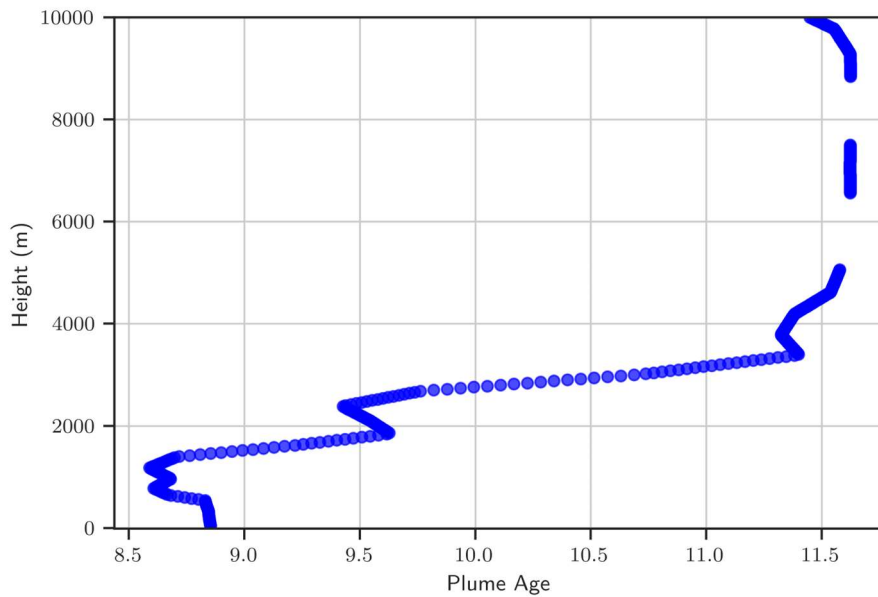

Figure S12(b): Vertical profile of plume age (mean of CO tracer concentrations) at Ascension on September 02, 2016, at 15:59 UTC.

17

The distribution of plume age on August 26, 2017, at 09:12:55 UTC is shown in Figure S13a, while the vertical profile of plume age is shown in Figure S13(b). The PBLH value (from WRF-CAM5) at the time is 1650m. The extinction-weighted aerosol age at the time is approximately 9 days in the TC and approximately 8 days in the FT.
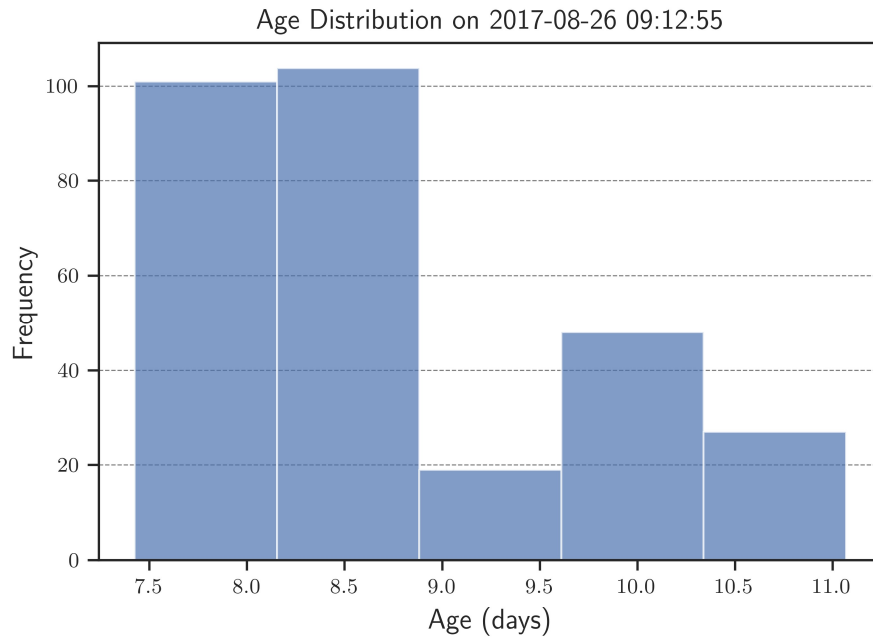

Figure S13(a): Distribution of plume age (mean of CO tracer concentrations) in the vertical at Ascension on August 26, 2017, at 09:12 UTC.
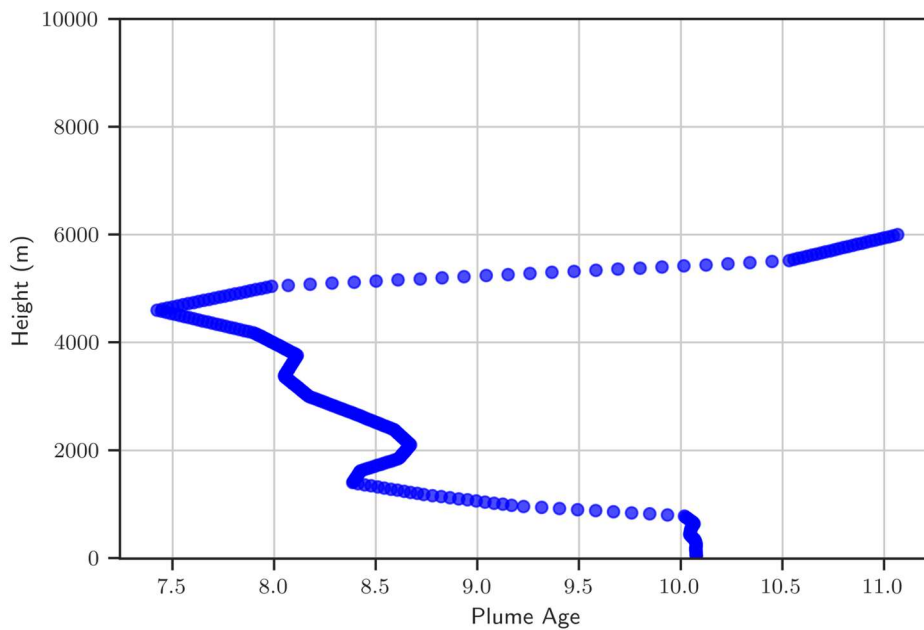

Figure S13(b): Vertical profile of plume age (mean of CO tracer concentrations) at Ascension on August 26, 2017, at 09:12 UTC.
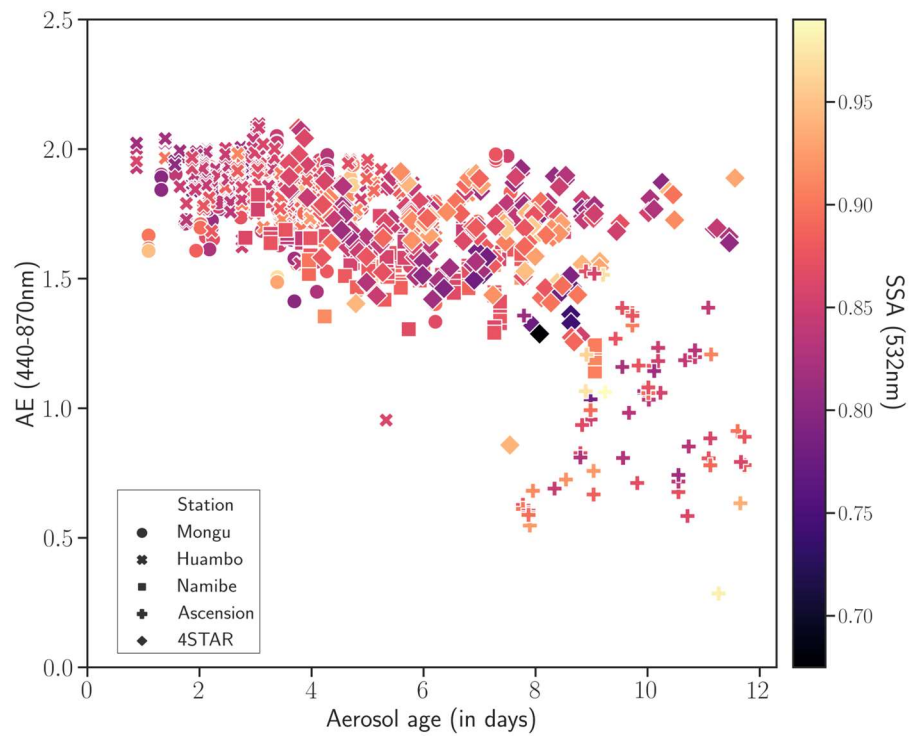
18

S6. AE Trend as a function of Age

Figure S14: Relationship between AE$_{440\text{-}870nm}$ (y-axis), SSA$_{532nm}$ (color bar), and aerosol age (x-axis) in the total atmospheric column (TC). The different markers represent the site of observation while the marker shading represents SSA.
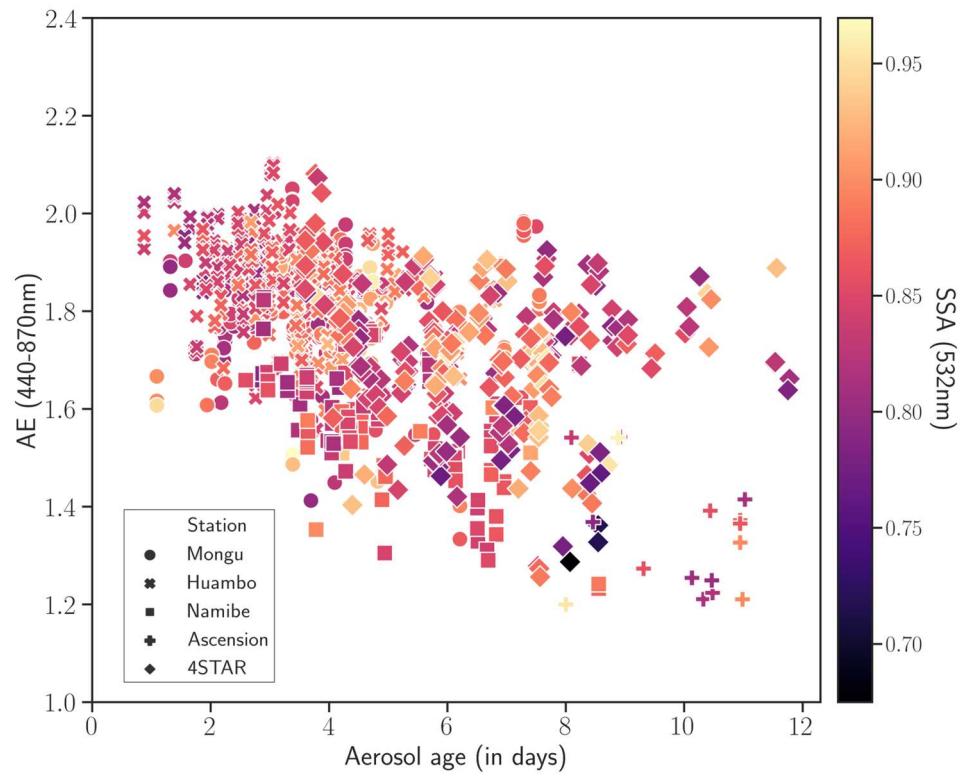
Figure S15: Same as Figure S14 but for free troposphere (FT) after filtering at AE≥1.2.

References

Dang, C., Segal-Rozenhaimer, M., Che, H., Zhang, L., Formenti, P., Taylor, J., Dobracki, A., Purdue, S., Wong, P. S., Nenes, A., Sedlacek Iii, A., Coe, H., Redemann, J., Zuidema, P., Howell, S., and Haywood, J.: Biomass burning and marine aerosol processing over the southeast Atlantic Ocean: a TEM single-particle analysis, Atmos. Chem. Phys., 22, 9389-9412, 10.5194/acp-22-9389-2022, 2022.

Dubovik, O. and King, M. D.: A flexible inversion algorithm for retrieval of aerosol optical properties from Sun and sky radiance measurements, Journal of Geophysical Research: Atmospheres, 105, 20673-20696, https://doi.org/10.1029/2000JD900282, 2000.

Eck, T. F., Holben, B. N., Reid, J. S., Dubovik, O., Smirnov, A., O'Neill, N. T., Slutsker, I., and Kinne, S.: Wavelength dependence of the optical depth of biomass burning, urban, and desert dust aerosols, Journal of Geophysical Research: Atmospheres, 104, 31333-31349, https://doi.org/10.1029/1999JD900923, 1999.

Eck, T. F., Holben, B. N., Reid, J. S., Mukelabai, M. M., Piketh, S. J., Torres, O., Jethva, H. T., Hyer, E. J., Ward, D. E., Dubovik, O., Sinyuk, A., Schafer, J. S., Giles, D. M., Sorokin, M., Smirnov, A., and Slutsker, I.: A seasonal trend of single scattering albedo in southern African biomass-burning particles: Implications for satellite products and estimates of emissions for the world's largest biomass-burning source, Journal of Geophysical Research: Atmospheres, 118, 6414-6432, 10.1002/jgrd.50500, 2013.

Eck, T. F., Holben, B. N., Reid, J. S., Sinyuk, A., Giles, D. M., Arola, A., Slutsker, I., Schafer, J. S., Sorokin, M. G., Smirnov, A., LaRosa, A. D., Kraft, J., Reid, E. A., O'Neill, N. T., Welton, E. J., and Menendez, A. R.: The extreme forest fires in California/Oregon in 2020: Aerosol optical and physical properties and comparisons of aged versus fresh smoke, Atmospheric Environment, 305, 119798, https://doi.org/10.1016/j.atmosenv.2023.119798, 2023.

Giles, D. M., Sinyuk, A., Sorokin, M. G., Schafer, J. S., Smirnov, A., Slutsker, I., Eck, T. F., Holben, B. N., Lewis, J. R., Campbell, J. R., Welton, E. J., Korkin, S. V., and Lyapustin, A. I.: Advancements in the Aerosol Robotic Network (AERONET) Version 3 database – automated near-real-time quality control algorithm with improved cloud screening for Sun photometer aerosol optical depth (AOD) measurements, Atmos. Meas. Tech., 12, 169-209, 10.5194/amt-12-169-2019, 2019.

Holben, B., Eck, T. F., Slutsker, I., Smirnov, A., Sinyuk, A., Schafer, J. S., Giles, D. M., and Dubovik, O.: Aeronet's Version 2.0 quality assurance criteria, Proc. SPIE, 10.1117/12.706524,

Holben, B. N., Eck, T. F., Slutsker, I., Tanré, D., Buis, J. P., Setzer, A., Vermote, E., Reagan, J. A., Kaufman, Y. J., Nakajima, T., Lavenu, F., Jankowiak, I., and Smirnov, A.: AERONET—A Federated Instrument Network and Data Archive for Aerosol Characterization, Remote Sensing of Environment, 66, 1-16, https://doi.org/10.1016/S0034-4257(98)00031-5, 1998.

Kumar, A., Pratap, V., Kumar, S., and Singh, A. K.: Atmospheric aerosols properties over Indo-Gangetic Plain: A trend analysis using ground – Truth AERONET data for the year 2009–2017, Advances in Space Research, 69, 2659-2670, https://doi.org/10.1016/j.asr.2021.12.052, 2022.

LeBlanc, S. E., Redemann, J., Flynn, C., Pistone, K., Kacenelenbogen, M., Segal-Rosenheimer, M., Shinozuka, Y., Dunagan, S., Dahlgren, R. P., Meyer, K., Podolske, J., Howell, S. G., Freitag, S., Small-Griswold, J., Holben,

B., Diamond, M., Wood, R., Formenti, P., Piketh, S., Maggs-Kölling, G., Gerber, M., and Namwoonde, A.: Above-cloud aerosol optical depth from airborne observations in the southeast Atlantic, Atmos. Chem. Phys., 20, 1565-1590, 10.5194/acp-20-1565-2020, 2020.

Sherman, J. P., Gupta, P., Levy, R. C., and Sherman, P. J.: An Evaluation of MODIS-Retrieved Aerosol Optical Depth over a Mountainous AERONET Site in the Southeastern US, Aerosol and Air Quality Research, 16, 3243-3255, 10.4209/aaqr.2015.09.0568, 2016.

Sinyuk, A., Holben, B. N., Eck, T. F., Giles, D. M., Slutsker, I., Dubovik, O., Schafer, J. S., Smirnov, A., and Sorokin, M.: Employing relaxed smoothness constraints on imaginary part of refractive index in AERONET aerosol retrieval algorithm, Atmos. Meas. Tech., 15, 4135-4151, 10.5194/amt-15-4135-2022, 2022.

Sinyuk, A., Holben, B. N., Eck, T. F., Giles, D. M., Slutsker, I., Korkin, S., Schafer, J. S., Smirnov, A., Sorokin, M., and Lyapustin, A.: The AERONET Version 3 aerosol retrieval algorithm, associated uncertainties and comparisons to Version 2, Atmos. Meas. Tech., 13, 3375-3411, 10.5194/amt-13-3375-2020, 2020.

Xu, Q., Obradovic, Z., Han, B., Li, Y., Braverman, A., and Vucetic, S.: Improving aerosol retrieval accuracy by integrating AERONET, MISR and MODIS data, 2005 7th International Conference on Information Fusion, 25-28 July 2005, 7 pp., 10.1109/ICIF.2005.1591916,

Zuidema, P., Sedlacek III, A. J., Flynn, C., Springston, S., Delgadillo, R., Zhang, J., Aiken, A. C., Koontz, A., and Muradyan, P.: The Ascension Island Boundary Layer in the Remote Southeast Atlantic is Often Smoky, Geophysical Research Letters, 45, 4456-4465, https://doi.org/10.1002/2017GL076926, 2018.